Performance Analysis of Gravitational Water Vortex Turbine using OpenFOAM

Amanuel Tesfaye* and A. Venkata Ramayya

Faculty of Mechanical Engineering, Jimma University, Jimma, Ethiopia

Abstract

A Gravitational Water Vortex Turbine is a new development that extracts power from artificially formed water vortex when the water from open flow channel directed tangentially to a round basin and discharges through the hole provided at the bottom of the basin. This can harness hydro power in application range of low to ultralow head and median to low flows and has the unique feature of leaving positive environmental impact through the aeration of water as it passes through the turbine. However, the presence of free–surface vortex in the flow field complicates its design from conventional impulse and reaction turbines perspective due to vortex-blade interaction.

Recent investigations have indicated that curved blade profiles are more efficient to harness the kinetic energy of the vortex. However, little amount of work has been done on the optimization of suitable runner for the free–surface vortex profile considering the vortex-blade interaction, the ratio of runner diameter to basin diameter (blade area) and its effect on torque and power output.

In this study, the performance of Gravitational Water Vortex Turbine has been investigated numerically using OpenFOAM. The effect of design parameters such as vortex-blade interaction, the ratio of runner diameter to basin diameter on the performance parameters such as effective head, torque, power and efficiency has been characterized. As a result, it is found out that a small blade size runner has higher rotational speed due to the strength of vortex was higher in the vicinity of air core but produces less torque. However, a large blade size runner has less rotational speed and high torque due to the nature of vortex tangential velocity field decrease with increasing radius and large blade area respectively. In addition, this work identified extending the size of runner blades to the far–field region resulting in reduction of power output. Therefore, the outcomes from this study will be helpful to design and establish performance analysis for the Gravitational Water Vortex Power Plant for a given flow and head of particular hydropower site. Moreover, it can also be used as pointer for the future generations of Gravitational Water Vortex Turbine technology.

Keywords: *Gravitational Water Vortex Turbine, Free-surface vortex, Vortex-blade interaction, Performance parameters, Air-core*

*Corresponding author: amanueltesfaye262@gmail.com

1 Introduction

Access to sustainable energy is a key pillar for daily activities of human being, economic growth, social development and poverty reduction. Despite population growth contribute an increase in energy demand, ensuring everyone has sufficient access to energy is still in progress and the most challenging issue over the world. Besides, the global energy consumption is dominated by fossil fuels which emit carbon dioxide (CO_2) and other greenhouse gases, the main cause for climate change. The climate change due to carbon footprint and depletion of fossil fuels, forcing individuals, private and governmental bodies to focus on the development of renewable energy technologies for ensuring everyone has sufficient access to sustain a high standard of life (Hoes et al., 2017).

Nowadays, these technologies have received much attention for providing global energy demand. International Energy Agency (IEA) reported renewables increased by 4% in 2018, accounting for almost one-quarter of global energy demand growth. Solar photovoltaic (PV), hydropower, and wind each accounted for about a third of the growth, with bioenergy accounting for most of the rest. Renewables covered almost 45% of the world's electricity generation growth, now accounting for over 25% of global power output (IEA, 2018). Solar and wind energy technologies are perfectly intermittent, they strongly depend on the availabilities of sun and wind of the place under consideration, whereas bioenergy can be utilized for replacing transportation fuels. From renewable energy technologies, hydropower is contributed the largest share for electricity generation, accounting for about 16.4% of the worlds net electricity production (REN21, 2018). Despite this, most of the available hydropower potential is still underutilized, where if exploited, it could replace a large amount of the contribution of electricity generation from fossil fuels (Timilsina et al., 2018).

Off-grid electrification is the main driver for the adoption of Mini, Micro, and Pico hydropower (MMPH) technologies, particularly in developing countries (World Bank, 2006). The selection of specific MMPH technology for implementation in remote areas depends on cost, ease of installation, portability, efficiency and maintenance (Williamson et al., 2014). Furthermore, there has been an attention towards low head ($5m - 20m$) technologies, which generally require lower capital cost,retain a lower spatial, and environmental footprint (Ramos et al., 2012).

Conventional turbines like Pelton, Crossflow and Francis turbines were found to be the most suitable for low head applications, but unsuitable when the hydraulic head is lower than $3m$. Their design and manufacturing are relatively complicated and expensive and requires large flow to maintain reliance efficiency. Moreover, common low head hydropower turbines like Archimedes Screw, water wheels, and modified conventional turbines have limited application ranges, due to poor part flow efficiency, manufacturing difficulties/cost, and uneconomical deployment (Rahman et al., 2016; Bajracharya et al., 2020).

The Gravitation Water Vortex Turbine (GWVT) is recently invented by Austrian Engineer,

Franz Zotlöterer in 2006, and is still emerging area for research (Timilsina et al., 2018). The Gravitational Water Vortex (GWVT) is an ultra-low-head ($< 5m$) technology which generates power from free-surface water vortex.

In the Gravitational Water Vortex Power Plant (GWVPP), the potential energy of water is converted to kinetic energy by round basin structure and this kinetic energy of water is extracted by a turbine placed in the center of the vortex as shown in Figure 1. The system mainly consists of a canal, a basin structure and the turbine. The water stream guided through a canal is tangentially fed into the round basin structure to form powerful water vortex due to induced circulation at the inlet and localized low pressure at the orifice (exit). The kinetic energy of the water vortex is converted to electrical energy through the turbine runner located in the center of water vortex. An exit hole is made at the bottom of the basin through which the water vortex discharges. Unlike most low head micro hydropower plants, this turbine does not work on the pressure differential across the turbine runner blades to create the torque on the output shaft, instead, it operates through the dynamic force of the vortex (Dhakal et al., 2017).

The main driver of interest in the GWVPP is its ability to generate hydropower for low to ultralow head ranges and median to low flows. In addition, the GWVPP is potentially a low environmental impact technology: compact in design where all the primary mechanisms are housed in the vortex chamber, operates at a low rotational velocity which does not harm aquatic and marine life, and aerates the water useful for the aquatic life which depletes the water quality (Rahman et al., 2017; Timilsina et al., 2018; Zotlöterer, 2020).

The proposed operating range of GWVPP in the generalized turbine application range by Timilsina et al. (2018) is shown in Figure 2. It indicates that the vortex hydropower plant (shaded area) has a rather larger operating envelope than Waterwheels and Archimedes screw turbines. In addition, compared to other hydroelectric generation technologies, the GWVPP have the greatest potential at low head sites and unlike conventional reaction or impulse turbines, they have the potential for maintaining high efficiencies even as the head approaches nearly zero or ultralow head (Williamson et al., 2014; Chattha et al., 2017).

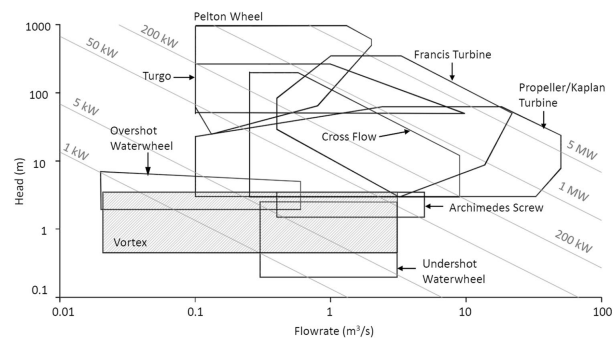**Figure 1:** *Basic components in a GWVPP (Source: Bajracharya et al. (2020)).*

Figure 2: *The application range of the vortex turbine (Source: Timilsina et al. (2018))*

.

The basin is one of the main parts of GWVPP used to induce artificial vortex which is responsible for the rotation of runner. The suitable basin configuration for the formation of stable and strong vortex flow depends on the form (shape) of the basin structure. As the GWVPP is a new technology, the design process of the basin structure is completely unknown and there is no scientific accepted shape of the basin. Several studies have been investigated on the geometrical structure of basin configuration with little variation in design. These are circular or traditional flat-based cylindrical basin (Zotlöterer, 2008; Mulligan and Casserly, 2010), scroll or spiral-type basin with flat base (Mulligan and Casserly, 2010; Mühle et al., 2013), stepped inlet (Zotlöterer, 2004; Bajracharya and Chaulagai, 2012), sloped inlet (Turbulent, 2020), conical basin (Marian et al., 2012; Dhakal et al., 2013, 2015), and concave and convex basin (Sánchez et al., 2019). Mulligan and Casserly (2010) and Mühle et al. (2013) identified that scroll or spiral-type vortex basin provides uniform flow distribution throughout the basin which results stable vortex. (Timilsina et al., 2018) reported that a cylindrical vortex basin tends to cause a distortion in the verticality of the vortex which can only be eliminated by shifting the bottom intake such that it is in line with the distorted central core. Alternatively, the stepped inlet basin can solve this by concentrating the inlet velocity near the free–surface of the vortex basin. This arrangement has problem for low flow conditions the water cascades into the vortex basin causing significant turbulence and a lack of coherent flow direction for a stable vortex to form. To resolve this, a sloped inlet can aid the transition of flows from smaller inlet channel into the vortex basin. However, for low flows again, the sloped floor causes the inlet flow to become supercritical and thus the water surface can slosh turbulently inside the basin under such conditions. The conical basin resolves the previous problems (Dhakal et al., 2015). The majority of large–scale deployments have been of the fat–based type (either cylindrical or scroll) while conical and stepped inlet type are yet to be practiced (Timilsina et al., 2018).

In addition to the shape of the basin, the formation of strong full air–core vortex depends on the size of the exit hole/orifice diameter (d). An experimental studies undertaken on the variation of orifice diameter (d) using a ratio of d/D where D was the uniform diameter of the vortex basin by Mulligan and Casserly (2010); Mulligan and Hull (2011); Mulligan et al. (2012) and concluded that optimum vortex strength occurs within the range of orifice to basin diameter (d/D) of $14\% - 18\%$, for low and high head sites, respectively. Moreover, Mulligan et al. (2018) extensively studied the flow field of full air–core strong free–surface vortex and categorized the vortex domain into two regions using the ratio of radial position to orifice diameter (r/d) namely: near–field (close to air–core) and far–field regions, for $r/d < 1$ and $r/d \geq 1$, respectively. The flow field tangential velocity distribution is strongly dependent on the axial flow conditions in the near–field region whereas the tangential velocity distribution was independent of the depth in the far–field region Mulligan et al. (2018).

Several studies have been investigated on the optimization of GWVT to improve the design and performance of the runner. A comparative study using CFD and experimental approach on

cylindrical and conical vortex basins showed that the output power and efficiency is maximum in the conical basin for the same flow conditions and additionally, the maximum power extraction was attained at the runner position of 65 – 75% of total height of basin from the top positions (Dhakal et al., 2015). Similarly, Marian et al. (2012); Dhakal et al. (2013); Kayastha et al. (2019) showed that a runner placed nearer to the outlet would harness power efficiently. An experimental study with a paddle–type runner was done by Rahman et al. (2016) by varying different design parameters: outer runner diameter, blade number, a blade length of the runner and showed that the maximum efficiency achieved with higher outer diameter. The study also identified the vortex turbine efficiency was can be affected by the blade length as well as the contact area between the turbine blades and vortex. Power et al. (2016) investigated an experimental parametric study for understanding the various operating conditions of the GWVPP. The study varied several design parameters such as the vortex height, inlet flow rates, inlet water height, runner blade sizes and blade numbers. From the experimental results, it was seen that the height of vortex decreases with an increase in blade area but the braking force increases, rendering the increase in power output thus the efficiency. A similar result was seen with increased blade numbers contributes to increase in efficiency which contradicts the finding by Dhakal et al. (2013), as the number of blades of turbine increased the efficiency of the GWVPP reduced. Moreover, the study showed that the overall maximum efficiency was recorded with the largest blade area, the maximum inflow rate. However, there might be an optimal number of blades and the ratio between blade sizes and basin diameter for the turbine.

The optimization of the runner blade profile was investigated using computational and experimental approach by Khan (2016) by considering four different blade profiles namely: inverted conical blades, crossflow blades, curved rectangular blades and twisted blades for comparison of their performance. The study showed that the maximum efficiency was obtained by using crossflow blades over other blade profiles for the same flow condition. Nishi and Inagaki (2017) conducted experiments and three dimensional unsteady, turbulent flow analysis by taking the free–surface into consideration using Volume of Fluid (VOF) approach. The Volume of Fluid (VOF) method is suitable for a flow field that has a clear interface between two phases (working fluids: water and air) and expresses the actual performance in a free–surface flow analysis of a water turbine, was also used. As a result, the experimental and the computational values of the torque, turbine output, and turbine efficiency and effective head agreed with one another.

The effect of inlet flow rate and approach channel (penstocks) geometry on performance of GWVPP was also by Rahman et al. (2018). It was discovered that increasing the width of the channel reduced the overall performance of GWVPP while the length of the channel has insignificant effects on the performance of turbine. Also, the performance of GWVPP improved along with increased inlet flow rate.

Ullah et al. (2019) investigated analytical and experimental study on the performance of a multi-stage gravitational water vortex turbine (GWVT). The GWVT stages are positioned

5

at different heights along the height of the conical basin designated as Bottom Stage (BS), Middle Stage (MS) and Top Stage (TS) based on distance from the bottom of the conical basin to the mid-height of the blades. Each runner of the multi-stage GWVT is independent in terms of power generation through telescopic shaft arrangement and the runner blade profiles similar to those of Savonius wind turbine blades (SWTBs) vertically attached to the hub. The comparison of experimental data amongst BS, MS and TS showed that the performance of the rotor positioned near upstream channel is higher than that of the rotors located below it, thereby indicating that surface vortex has more energy available for power generation because it remains undistorted before its contact with TS. The highest power attained is maximum at TS, minimum at MS and intermediate at BS of the multi-stage GWVT.

In general, different authors used different blade profiles and number of blades for GWVPP in their investigations which indicates the concept of GWVPP has not been well developed and no generic design approaches or manuals available to allow one to design and establish expected performance for the GWVPP for a given flow and head of hydropower site. Additionally, most studies found that curved blade profiles are more efficient to harness the kinetic energy of the vortex (Khan (2016); Kueh et al. (2017); Ullah et al. (2019)). To the best of authors' understanding, little amount of work has been done on the optimization of suitable runner for the free–surface vortex profile considering the vortex-blade interaction, the ratio of runner diameter to basin diameter (blade size) and its effect on torque and power output. Therefore, the present study mainly focuses on optimization of suitable runner for GWVPP to characterize the effect of design parameters such as vortex-blade interaction, the ratio of runner diameter to basin diameter on the performance parameters such as effective head, torque, power and efficiency.

2   System design and analysis

A Gravitational Water Vortex Power Plant mainly consists of a basin and a turbine with blades. The basin is a large round cross section to generate an artificial gravitational water vortex. The turbine may have a single or multiple stage of runners. The present study has considered a scroll basin and a single-stage turbine setup. The design of each of these components have been described as follows:

2.1   Scroll basin

Scroll or spiral-type vortex basin provides uniform flow distribution throughout the basin which results stable vortex (Mulligan and Casserly, 2010; Mühle et al., 2013). The basin structure is known as spiral-type basin (Drioli chamber) commonly used for a vortex drop shaft (Drioli, 1947). It is around chamber that consists of circle parts with varying radii which are smoothly connected as shown in Figure 3.
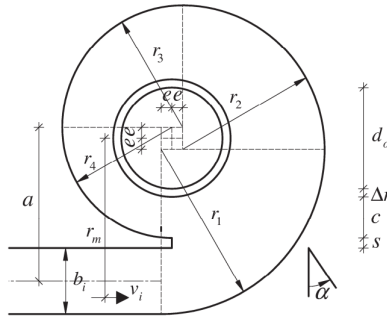
Figure 3: Construction scheme according to Drioli (Source: Mühle et al. (2013))

According to Drioli's design consists of four different radii. The center of those radii is displaced by an eccentricity factor e from the middle of the outlet opening. For calculating the eccentricity factor e and the different radii the following equations can be used (Drioli, 1947)

$$e = \frac{1}{7}(b_i + s), \qquad r_1 = \frac{1}{2}d_o + 6e + \Delta r + c, \qquad r_2 = r_1 - 2e, \qquad r_3 = r_1 - 4e \qquad r_4 = r_1 - 5e \quad (1)$$

The distance from the center of orifice to the middle of the inlet channel is required for the relation of the flow depth, the discharge and induced circulation, it can be calculated with Eq. (2).

$$r_{in} = r_1 + e + \frac{b_i}{2} \tag{2}$$

The values for b_i, d_o, Δr, s and c have to be determined to calculate the geometric dimensions of the scroll vortex chamber. The parameter c defines the distance between the outlet opening and the construction to the inlet. For a drop shaft it should be kept small for a compact shaft. But for the vortex hydropower plant a higher value is needed, because c influences the mean diameter of the basin which should be greater in the plant so that there is an area with lower velocities in the outer range of the basin where the fish and other aquatic life's can pass by unharmed.

In this study a scroll basin is designed for an approach flow condition of 0.00386 $(m^3\ s^{-1})$ through a channel width (b_i) of 80 mm and channel depth (h) of 250 mm. According to Mühle et al. (2013) the width of the inlet should have the same size as the orifice diameter $b_i \approx d_o$. The basin diameter was obtained as 500 mm by taking the ratio of orifice diameter to basin diameter to be 16%. Figure 4 and Table 1 provides a schematic and tabulated description of the designed basin configuration. Using the specifications in Table 1, a 3D model was developed by FreeCAD and shown in Figure 5.
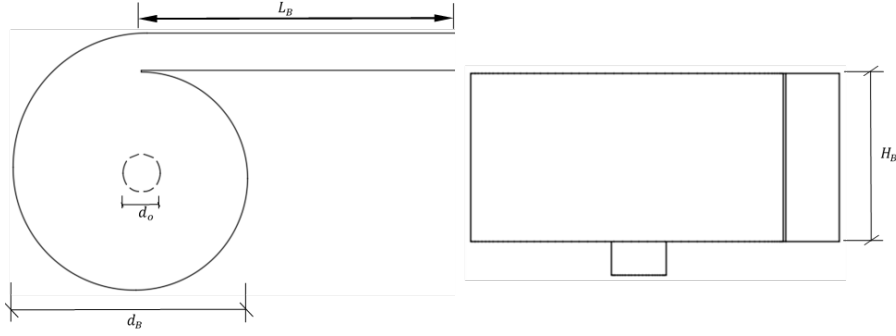
Figure 4: *Plan of scroll basin configuration on horizontal and vertical planes*

Table 1: *Specifications of basin configuration*

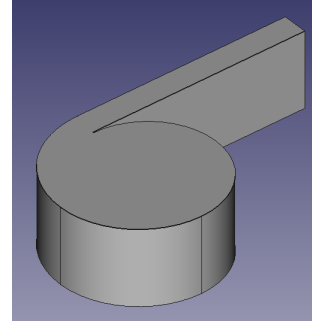| Basin parameters	
Basin diameter (d_B)	500 mm
Orifice diameter (d_o)	80 mm
Ratio of basin diameter to orifice diameter (d_o/d_B)	0.16
Basin height (H_b)	250 mm
Inlet channel width (b_i)	80 mm
Inlet channel length from center vertical axis (L_B)	700 mm
Orifice length (L_o)	50 mm

Figure 5: *Scroll basin 3D model developed in FreeCAD*

2.2   Gravitational Water Vortex Turbine

Much attention has been paid in the previous studies to the design of the runner blade profiles and found that curved blade profiles are more efficient to harness the kinetic energy of the vortex (Khan, 2016; Kueh et al., 2017; Ullah et al., 2019). The design of the blade profile in the present study is similar with cross–flow (centrifugal) type where the gravitational water vortex flow has been modeled as a jet of water striking the blades of gravitational water vortex runner. The tangential velocity strikes the tip of the blade (center of the curved plate as a tip). The blades are distributed circumferentially, wherein the rotation axis of the runner coincides with the vertical axis through the center of orifice. Figure 6 shows illustrative model of cross-flow (centrifugal) type runner used in the current study.
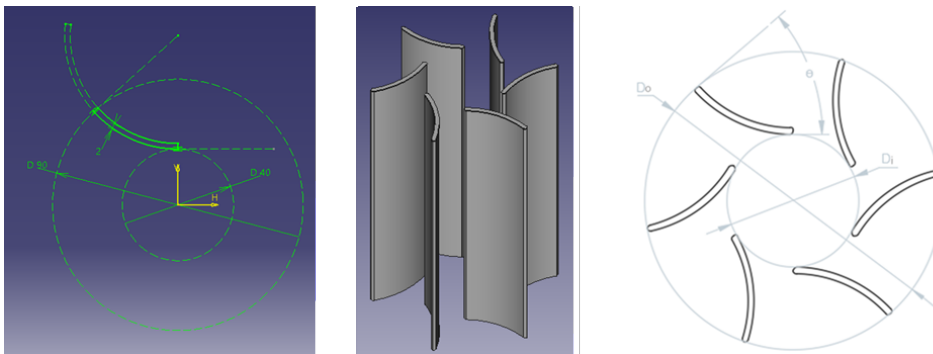

Figure 6: *Sketch and 3D model view of the runner*

The runner blade profiles are specified by the radius of curvature (r_c) and deflection angle (θ) between tangent lines at the blade inlet and blade outlet by using Equation (3).

$$r_c = \frac{r_o^2 - r_i^2}{2r_i} \qquad and \qquad \theta_c = 90 - \tan^{-1}\left(\frac{r_o}{r_c}\right) \tag{3}$$

where $r_o = D_o/2$ and $r_i = D_i/2$.

In the present study, the runner outer diameter is varied from $D_o = 90$ mm, 135 mm, and 180 mm to investigate the influence of runner diameter to basin diameter ratio on performance parameters of the runner. The runner inner diameter is $D_i = 40$ mm, blade height is $B_h = 140mm$, blade thickness is $B_t = 2$ mm, and number of blades is $Z = 6$. The runner is placed with a clearance of $\delta = 5$ mm between the basin base and runner base. The detail specification and description of each type of the runner blades are shown in Table 2 and Figure 7.

Table 2: *Specification of runner types with their blade profile*

| Design Parameters	Runner type		
	Runner A	Runner B	Runner C
Runner outer diameter (D_o)	90 mm	135 mm	180 mm
Runner inner diameter (D_i)	40 mm	40 mm	40 mm
Runner diameter to Basin diameter ratio (R)	0.18	0.27	0.36
Runner blade height (B_h)	140 mm	140 mm	140 mm
Runner blade thickness (B_t)	2 mm	2 mm	2 mm
Blade radius of curvature (r_c)	40 mm	104 mm	192 mm
Blade deflection angle (θ_c)	42 deg	57 deg	65 deg
Number of blades (Z)	6	6	6
Clearance between basin base and runner base (δ)	5 mm	5 mm	5 mm
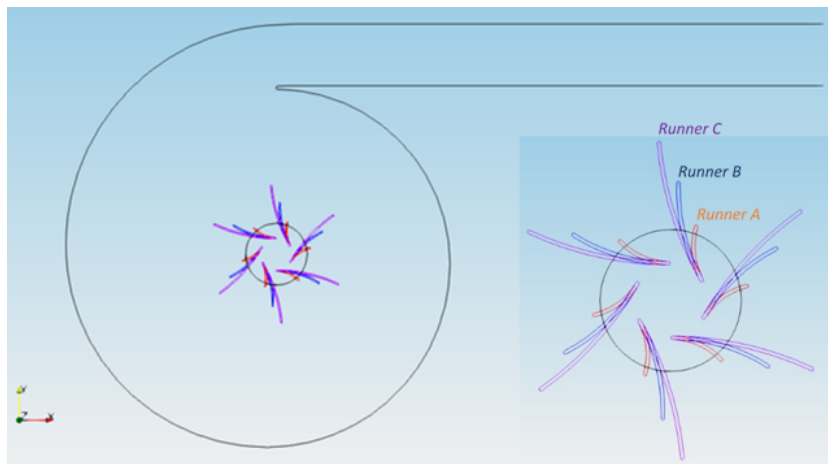
Figure 7: *Variation of runner outer diameter*

2.3 Hydraulic power

The potential of hydropower development is determined by the available energy head (m) and the flow (m^3/s) of a river. For any hydropower turbine, the theoretical hydraulic power input was determined by Eq. (4):

$$P_{in} = \rho g Q H_n \tag{4}$$

where H_n is the effective (net) head at the site and Q is the flow rate passing through the turbine. However, the net head is given by:

$$H_n = H_g - H_l$$

where H_g is the gross head and H_l is total head losses along the radius, at the orifice or intake and the kinetic energy of the outflow (Timilsina et al., 2018).

In Gravitational water vortex power plant, water from the approach channel is fed tangentially into a vortex chamber inlet point $\boxed{1}$ which sets up conditions of strong circulation to drive the runner shaft aligned with an axis through the center of orifice $\boxed{2}$. After creating torque on the shaft, the water discharges from orifice point $\boxed{2}$ to an outlet point $\boxed{3}$.

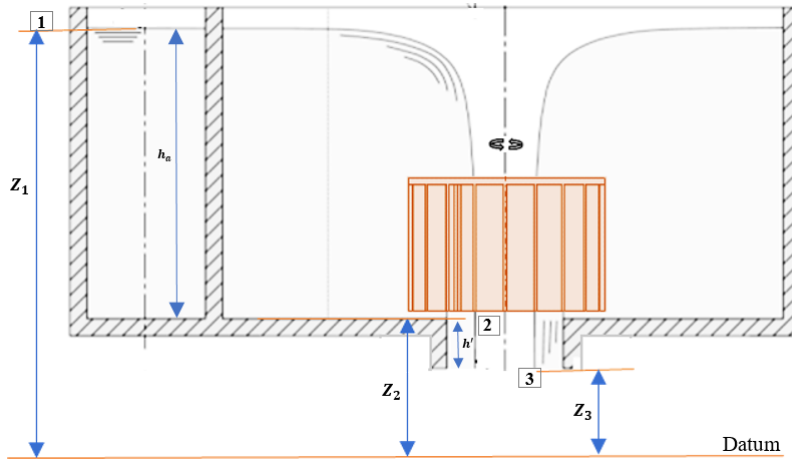**Figure 8:** *System analysis for GWVPP*

In the control volume shown in Fig. 8, the system produces shaft work between point $\boxed{1}$ to $\boxed{2}$ and free outflow from point $\boxed{2}$ to $\boxed{3}$. Therefore, the conservation of energy principle applied for the flow between the point $\boxed{1}$ to point $\boxed{2}$ and the Bernoulli's principle for the flow from point $\boxed{2}$ to point $\boxed{3}$.

Applying conservation of energy principle for the flow between the points $\boxed{1}$ and point $\boxed{2}$ by taking the consideration of steady, incompressible, inviscid and adiabatic (no thermal energy involved) fluid flowing through the system, results in 5:

$$\frac{p_1}{\rho g} + \frac{V_1^2}{2g} + Z_1 = \frac{p_2}{\rho g} + \frac{V_2^2}{2g} + Z_2 + H_t \tag{5}$$

10

where H_t is turbine work head or effective head H_n.

For the fluid flow from orifice point $\boxed{2}$ to outlet point $\boxed{3}$, the Bernoulli's principle applied because neither thermal energy nor shaft work are within the zone, given by:

$$\frac{p_2}{\rho g} + \frac{V_2^2}{2g} + Z_2 = \frac{p_3}{\rho g} + \frac{V_3^2}{2g} + Z_3 \tag{6}$$

By combining Eq. (5), Eq. (6) and substituting zero pressure (free to atmosphere) for p_1 & p_3, the effective or net head can be obtained by Eq. (7):

$$H_n = \frac{V_1^2 - V_3^2}{2g} + Z_1 - Z_3 = h_a + h^{'} + \frac{V_{in}^2 - V_{out}^2}{2g} \tag{7}$$

where h_a is the approach (upstream channel) water depth and $h^{'}$ is the difference in height between the bottom surface of tank and the outlet.

2.4 Mechanical power

A turbine transforms kinetic and pressure energy into mechanical power. The water that runs through the turbine is deflected by the turbine blades will cause a force in rotational direction that produces torque. This torque spins a generator which transforms the mechanical power into electrical power.

With the torque (T) and the angular velocity (ω) of the turbine, the mechanical power output can be obtained by Eq. (8):

$$P_{out} = T\omega \tag{8}$$

However, the rotational speed (N) and the angular velocity (ω) of the turbine was related using the following equation:

$$\omega = \frac{2\pi N}{60} \tag{9}$$

Therefore, the hydraulic turbine efficiency can be calculated by Eq. (10):

$$\eta_t = \frac{P_{out}}{P_{in}} \tag{10}$$

3 Numerical Analysis

Experimental studies have drawbacks such as being costly, laborious, time-consuming as well as issues about the scale effects. The numerical study approaches through the use of Computational Fluid Dynamics (CFD) tools able to address some of these challenges. Furthermore, problems with scaling do not arise as CFD models can be set up at realistic scale if needed. However, the results from CFD studies require validation with experimental or analytical models before they can be used for design purposes by considering physical approximation, computer

round-off, iterative convergence and discretization errors into account (Ferziger and Peric, 2002; Versteeg and Malalasekera, 2007).

In CFD simulations, the fluid problems are handled by solving the fluid flow equations (i.e. Navier-Stokes equations) in their discretized form, thus providing a spatial and time-dependent solution for the problem under investigation (Timilsina et al., 2018). In this work an open source CFD package (OpenFOAM) is selected to simulate the flow field of GWVPP. Like any other commercial CFD package, OpenFOAM is based on finite volume method and it contains utilities for handling the whole CFD workflow i.e. pre-processing, solving and post-processing. Compared to commercial packages, OpenFOAM has several advantages. It is free of charge and has open source code. Therefore, the end user can check the implementation of a theoretical model directly in the code which helps the user for better understanding how a solver works.

The Volume of Fluid (VOF) method introduced by Hirt and Nichols (1981) is suitable for multiphase flow problems, which has a clear interface between two phases (working fluids: water and air) and expresses the actual performance a free surface flow analysis of a GWVT Müller et al. (2018); Nishi et al. (2020). OpenFOAM uses *interFoam* solver, a pre-written solver for two incompressible, isothermal immiscible fluids using a volume of fluid (VOF) phase-fraction based interface capturing approach, with optional mesh motion and mesh topology changes including adaptive re-meshing (Christopher, 2018).

Governing equations

The governing equations are the mass conservation equation – Eq. (11), momentum conservation equation – Eq. (12) and volume conservation equation – Eq. (13) with Reynold Averaged Navier–Stokes (RANS) the most commonly used turbulence model for practical and industrial applications. The RANS equations implement the Reynolds decomposition of flow parameters such that $\mathbf{u} = \bar{\mathbf{u}} + \mathbf{u}'$ and $p = \bar{p} + p'$.

$$\nabla.\bar{\mathbf{u}} = 0 \tag{11}$$

$$\frac{\partial(\rho\bar{\mathbf{u}})}{\partial t} + \nabla.(\rho\bar{\mathbf{u}}\bar{\mathbf{u}}) = -\nabla\bar{p} + \rho\mathbf{g} + \nabla.\left[\mu_{eff}\left(\nabla\bar{\mathbf{u}} + (\nabla\bar{\mathbf{u}})^T\right)\right] + \mathbf{F_s} \tag{12}$$

$$\frac{\partial\alpha}{\partial t} + \nabla.(\alpha\bar{\mathbf{u}}) = 0 \tag{13}$$

where $\mathbf{u}$ is the velocity, $\bar{\mathbf{u}}$ is the time–averaged velocity, $\mathbf{u}'$ is the velocity fluctuation, p is the pressure, $\bar{p}$ is the time–averaged pressure, p' is the pressure fluctuation, α is the volume fraction which ranges from 0 to 1 (with cells fully filled gas assigned a value of 0 whilst cells fully filled with liquid are assigned a value of 1; the location of the interface is captured by cells with volume fraction $0 < \alpha < 1$), $\mathbf{g}$ is the acceleration due to gravity, μ_{eff} is the effective viscosity, $\mathbf{F_s}$ is the surface tension force.

The density (ρ) and viscosity (μ) of the fluid are expressed by the following relations in Eq. (14) and Eq. (15). The subscripts l and g in the equations refer to liquid and gas respectively.

$$\rho = \alpha\rho_l + (1 - \alpha)\,\rho_g \tag{14}$$

$$\mu_{eff} = (\mu_{eff})_l\alpha + (\mu_{eff})_g\,(1 - \alpha) \tag{15}$$

In order to address challenges associated with numerical diffusion at the interface region as well as to attain a sharp interface, OpenFOAM implements an artificial velocity $\mathbf{\bar{u}_r}$ which modifies 13 to obtain Eq. (16) (Santiago, 2004).

$$\frac{\partial\alpha}{\partial t} + \nabla.\,(\alpha\mathbf{\bar{u}}) + \nabla.\,[\alpha\,(1 - \alpha)\,\mathbf{\bar{u}_r}] = 0 \tag{16}$$

where $\mathbf{\bar{u}_r} = \mathbf{\bar{u}}_l - \mathbf{\bar{u}}_g$ is the vector of relative velocity between the two fluids, also called as compression velocity (artificial compression term). Additionally, the pressure gradient must be different for each phase due to the hydrostatic component ($\rho\mathbf{g}$) when the phases are separated at the wall. A modified pressure $\bar{p}^*$ (p_rgh in OpenFOAM) is defined to remove the hydrostatic pressure ($\rho\mathbf{g}.\mathbf{h}$) as:

$$\bar{p}^* = \bar{p} - \rho\mathbf{g}.\mathbf{h} \tag{17}$$

where $\mathbf{h}$ is the position vector. Considering the modified pressure, the momentum equation (Eq. (12)) is also modified to Equation (18).

$$\frac{\partial\,(\rho\mathbf{\bar{u}})}{\partial t} + \nabla.\,(\rho\mathbf{\bar{u}\bar{u}}) = -\nabla\bar{p}^* + \nabla.\,\left[\mu_{eff}\left(\nabla\mathbf{\bar{u}} + (\nabla\mathbf{\bar{u}})^T\right)\right] - \mathbf{g}.\mathbf{h}\nabla\rho + \mathbf{F_s} \tag{18}$$

where $\mathbf{F_s} = \sigma\kappa\nabla\alpha$, σ is the surface tension at the liquid–gas interface and κ is the mean curvature of the free–surface which obtained by $\kappa = -\nabla.\mathbf{n} = -\nabla.\left(\frac{\nabla\alpha}{|\nabla\alpha|}\right)$.

Therefore, the final form of the mathematical models used in interFoam solver are the continuity equation (Eq. (11)), phase transport equation (Eq. (16)) and the momentum equation (Eq. (18)). These equations are solved together with the constitutive relations for density, dynamic viscosity and velocity in the interface region.

Turbulence modeling

In this study, the Reynolds–Averaged Navier–Stokes (RANS) and two–equation $k-\omega$ SST with curvature correction are employed for the analysis of GWVT due to its good behavior in adverse pressure gradients, rotating and separating flow. Furthermore, it provides robustness with lesser computational time than the Reynolds Stress Model (RSM) for vortical flow simulation (Mulligan et al., 2016; Bajracharya et al., 2020), since the SST $k-\omega$ model blends $k-\omega$ in the near–wall region and $k-\varepsilon$ in the free stream (Menter et al., 2003).

In the $k - \omega\ SST$ model, the viscosities used in Equation (15) are obtained from Equations (19) to (21).

$$\mu_{eff} = \mu + \mu_t \tag{19}$$

$$\mu_t = \frac{a_1 \rho k}{\max\left(a_1 \omega, \overline{S} F_2\right)} \tag{20}$$

$$F_2 = \tanh\left[\left(\max\left(\frac{2\sqrt{k}}{\beta^* \omega y}, \frac{500\nu}{y^2 \omega}\right)\right)^2\right] \tag{21}$$

where μ refers to the viscosity of the fluid, μ_t is the turbulent viscosity, k is the turbulent kinetic energy, ω is the specific rate of dissipation of turbulence kinetic energy, a_1 is the model coefficient which equals 0.31, $\overline{S}$ refers to the strain rate magnitude, F_2 represents the blending function which is computed using Eq. (21) and $\beta^* = 0.09$ (Menter et al., 2003). Additional transport equations for the turbulent kinetic energy (k) and the specific dissipation rate (ω) can be obtained from Menter et al. (2003).

The $k - \omega\ SST$ with Curvature Correction (CC) model was developed by Smirnov and Menter (2009). In this CC model, the production terms of the k and ω equations, are multiplied by f_{r1} function,

$$f_{r1} = \max\left(\min\left(f_{\text{rotation}}, 1.25\right), 0\right) \tag{22}$$

where

$$f_{rotation} = (1 + C_{r1})\frac{2r^*}{1 + r^*}\left[1 - C_{r3}\tan^{-1}\left(C_{r2}\widehat{r}\right)\right] - C_{r1}$$

In this equation, r^* and $\widehat{r}$ are defined as,

$$r^* = \frac{\left|\overline{S}\right|}{\left|\overline{\Omega}\right|} \qquad and \qquad \widehat{r} = \frac{2\overline{\Omega}_{ik}\overline{S}_{ik}}{\left|\overline{\Omega}\right|\overline{D}^3}\frac{D\overline{S}_{ij}}{Dt}$$

where

$$\overline{D}^2 = \max\left(\overline{S}^2, 0.09\overline{\Omega}^2\right), \qquad \overline{S}^2 = 2\overline{S}_{ij}\overline{S}_{ij}, \qquad \overline{\Omega}^2 = 2\overline{\Omega}_{ij}\overline{\Omega}_{ij}$$

Note that in this model, the non-dimensional forms of the strain and rotational rate tensors are not used. The coefficients of this model are $(C_{r1}, C_{r2}, C_{r3}) = (1.0,\ 2.0,\ 1.0)$.

The official OpenFOAM distribution from OpenFOAM foundation does not include the curvature correction in any existing turbulence models. However, the standard kOmegaSST model proposed by Smirnov and Menter (2009) was modified to kOmegaSSTCC turbulence model under supervision of TotalSim Ltd and available for public under GitHub distribution (https://github.com/ancolli/kOmegaSSTCC).

Multiple Reference Frame (MRF)

The CFD simulation for rotating machinery is implemented by Multiple Reference Frame (MRF) method to minimize the computational time (Wilhelm, 2015). A comparative study between Sliding Mesh (SM) and Multiple Reference Frame (MRF) approaches for Francis turbine simulation has been investigated and concluded that SM does not offer a significant advantage over the MRF approach for overall turbine characteristics prediction (Tonello et al., 2017). Gullberg and Sengupta (2011) also suggested that the MRF technique can provide an accurate prediction of turbomachinery performance. Both of the studies conclude that the SM approach is more accurate than the MRF approach; however, turbine/pump performance can be accurately predicted by MRF alone. Also, SM is more useful for understanding flow regimes, pressure fluctuation, etc. in the vicinity of the impeller. Thus, MRF was chosen for this study to predict turbine performance.

Numerical solution procedure

The *interFoam* solver uses the finite volume method to discretize the governing equations. The *Euler* differencing scheme was used for temporal discretization with *adjustableTimeStep* by setting *maxAlphaCo* and *maxCo* to 1 (CFL - criteria) which is necessary for stability of the simulation in the PIMPLE algorithm. The gradient schemes was discretized by *leastSquares* method and Second order accuracy discretization schemes have been selected for the divergence terms. Additionally, limiters are coupled to achieve better stability in regions of strong gradients. The *limitedLinearV* scheme was used for U whilst *linearUpwind* scheme was selected for the divergence related to turbulence terms. For the divergence of alpha and for the compression of the interface, the *vanLeer* and the *interfaceCompression* schemes were used, respectively. For the Laplacian schemes, the *Gauss linear* corrected scheme was implemented (Christopher, 2018).

CFD Modelling

In this study, the CFD analysis was performed for the performance of GWVT located in the center of artificially water vortex formed by the scroll basin. The CFD analysis was based on multiphase VOF approach where two fluids, air and water (Newtonian fluids), occupy same domain. The fluid properties of was found from standard table at a domain temperature 20^oC. The constant gravitational acceleration of 9.81 m/s^2 acting downward (negative z-direction) in the domain. The $k - \omega$ SST–CC turbulence model was selected for the simulation.

The computational domain is contains two fluid domains namely: stationary fluid domain (basin domain) and rotating fluid domain (runner domain). The runner blade boundary walls are bounded inside the runner domain and its rotational speed was an input parameter for the CFD analysis (Regmi et al., 2019). The geometry of the models was built in FreeCAD and SALOME to extract physical boundary surfaces from the 3D models. The physical boundary

15

surfaces of the system are shown in Figure 9, which contains five patches namely: inlet, outlet, basin walls, atmosphere and bladeWalls. The domain is initially filled with air and the flow is developed from the inlet until quasi steady-state. At the basin inlet, an open-channel inflow boundary condition was imposed by defining the volumetric flow rate value. Free to atmosphere outflow boundary condition is used at outlet of the basin. At the basin wall boundaries, a no-slip (fixed velocity of zero) condition was imposed on the velocity field with wall functions for turbulence variables. The top surface of the domain is also treated as atmospheric boundary patch. Moreover, bladeWalls patch represents the wall boundary surfaces of the runner blades where water stream passing through the runner acting forces on the blade surfaces of the runner resulting in the torque about the rotational axis.
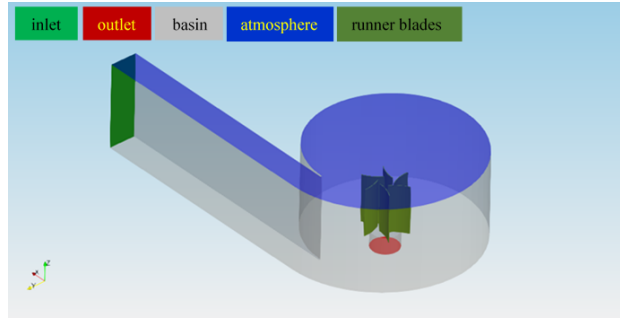

Figure 9: *Physical boundaries of the computational domain for scroll basin with runner*

The boundary conditions used for the simulation are provided in Table 3.

Table 3: *Boundary conditions used in the OpenFOAM simulations*

Physical surface	Flow properties					
	alpha.water	k	nut	omega	p_rgh	U
inlet	variableHeight FlowRate 0	fixedValue 0.000125	calculated	fixedValue 2.4267	fixedFlux Pressure	variableHeight FlowRateInlet Velocity 0.00386
outlet	zero Gradient	zero Gradient	zero Gradient	zero Gradient	prghTotal Pressure	zero Gradient
atmosphere	inletOutlet 0	inletOutlet 0.000125	calculated	inletOutlet 2.4267	prghTotal Pressure	pressureInlet OutletVelocity
walls	zero Gradient	kqRWall Function	nutkWall Function	omegaWall Function	fixedFlux Pressure	fixedValue (0 0 0)
bladeWalls	zero Gradient	kqRWall Function	nutkWall Function	omegaWall Function	zero Gradient	movingWall Velocity (0 0 0)

The computational domain was meshed using the open source meshing tool snappyHexMesh and shown in Figure 10. The simulation was run on 8 cores (Intel Core i7 @ 3.6 GHz) of a desktop computer with 8 GB RAM. A normalized residual value of order 1×10^{-4} was used for convergence criteria. The numerical results were post-processed in ParaView for visualisation

after the end of the simulation. In addition, OpenFOAM uses run–time post–processing utilities. The built–in forces function calculates forces and torques by integrating the pressure and skin skin–friction forces over a given list of patches (Foundation, 2020). The output is given in columns containing time, pressure and viscous forces, and torque due to pressure and viscous forces. Both force and torque are decomposed in the x –, y – and z – directions. In this study the runner rotates about z – axis, the total torque of the runner is the sum of the pressure and viscous moments in the z–direction. It should be noted that the simulation cases are computed until the solution becomes in quasi steady-state condition. Therefore, the data analysis will be done by the average value in the quasi steady-state condition.
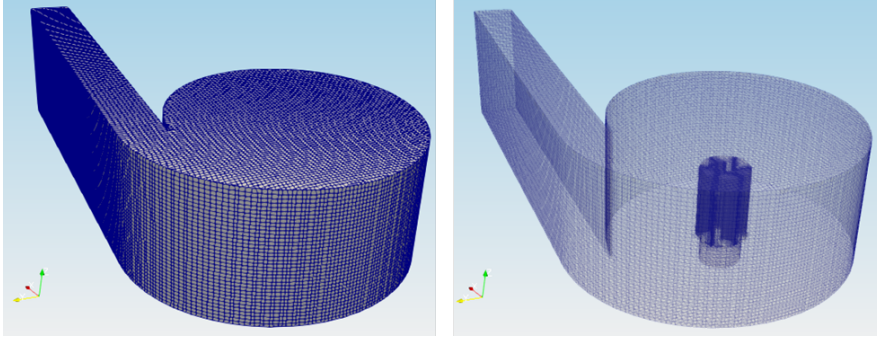
Figure 10: *Computational mesh for both stationary and rotating fluid domain*

For any CFD result to be less erroneous, it is required that the solution converges and the required solution parameter/s become independent of number of divisions the fluid domain is divided into (Freitas, 2002). The mesh independence test is shown in Figure 11 for the computational domain with four mesh resolutions: *60,981*, *122,091*, *213,544* and *337,552* number of cells. The simulations were computed for Runner A at a rotational speed of 45 rpm. This shows that the output torque is sensitive to the number of cells of the computational domain. The difference between two consecutive high resolution meshes is *0.96%*. This suggests that a computational domain with *337,552* number of cells is satisfactory and the cell size for *337,552* number of cells used for all simulation cases.
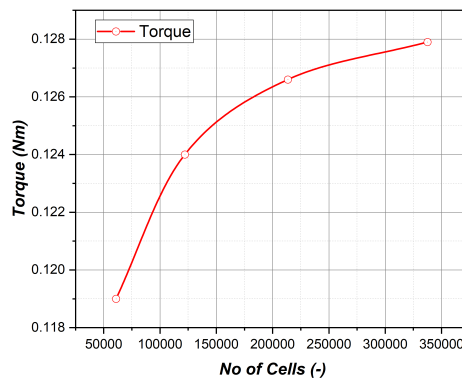

Figure 11: *Mesh independence for Runner A at N = 45 rpm*

17

4 Results and discussion

In this section the results of CFD analysis for runner optimization were presented and discussed. The optimization of runner was performed by investigating the influence of design parameters on performance parameters of the runner. The design parameters are vortex–blade interaction, the size of runner specified by runner outer diameter whilst the performance parameters of the runner are Torque, Power output, Effective head and Efficiency analyzed from CFD results by Equations (7), (8) and (10) discussed in Section 2.

Before analyzing the influence of design parameters on performance parameters, three simulations were performed for Runner A, Runner B and Runner C in scroll basin using the selected mesh size from the mesh sensitivity analysis. Similar turbulence model, boundary conditions and initial values, flow condition are employed for all simulations, while runner rotational speed is an additional input applied for the rotating domain in the simulations. All simulations are employed in scroll basin having 500 mm. However, the fluid flow analysis is transient where the computational domain is initially filled with air and the water flow is developed from the inlet indicates that the output torque is also time dependent until quasi steady state condition obtained. Therefore, the convergence process for total torque due to pressure and viscous forces of the fluid on runner blade walls are monitored during the simulations using built–in forces function and plotted by OpenFOAM built–in software GNUPLOT as shown in Figure 12. The simulations are computed at the same rotational speed value of 45 rpm for the total physical time of 50 seconds. The scatter data on Figs. 12a to 12c represent output torque values obtained at each write time, while the lines represent average torque values.
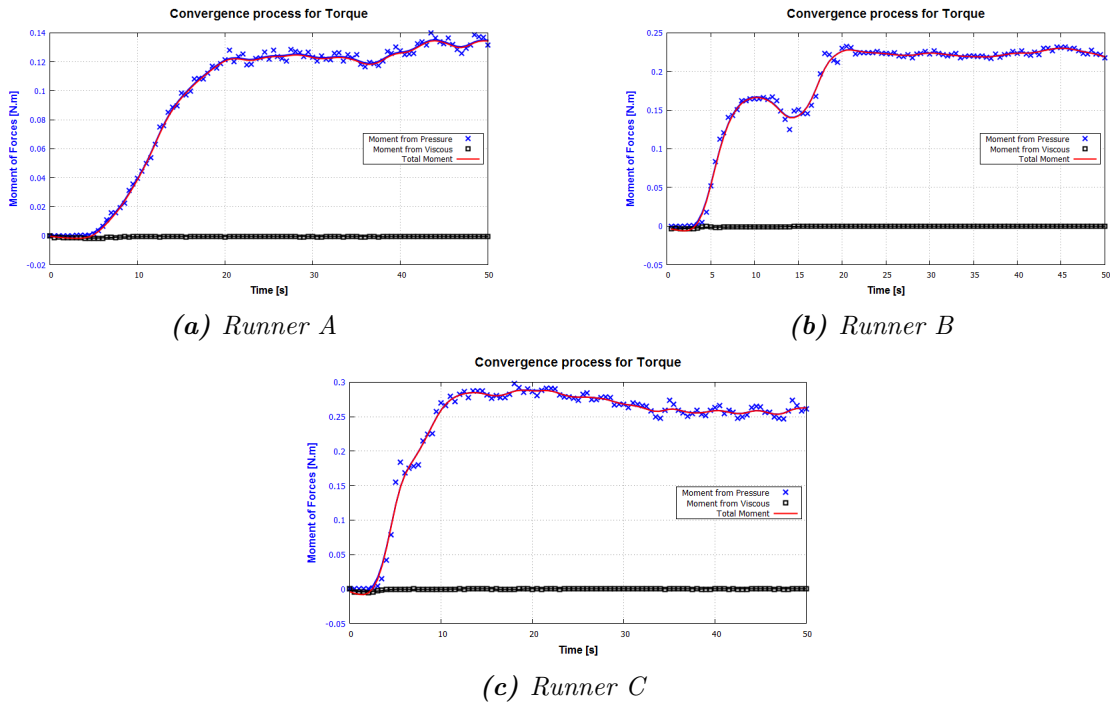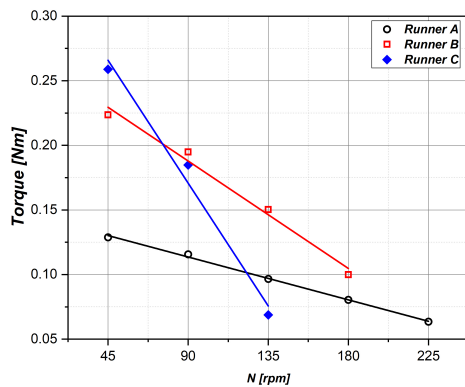

(a) Runner A

(b) Runner B

(c) Runner C

Figure 12: *Transient analysis of output torque at $N = 45\ rpm$*

18

The CFD results show that torque is generated after few seconds which means the water flow in the basin domain reach the runner blades after few seconds. Between 5 seconds and 10 seconds the torque generated is dependent on time and increase with steeper gradient in Runner C as compared with Runner A and Runner B. The transient behavior of the simulations reached quasi-steady state condition beyond 20 seconds for Runner A and Runner B while 12 seconds for Runner C. For all simulation cases, the variables used in performance parameters are analyzed by taking the average of data in the range between 25 - 50 seconds.
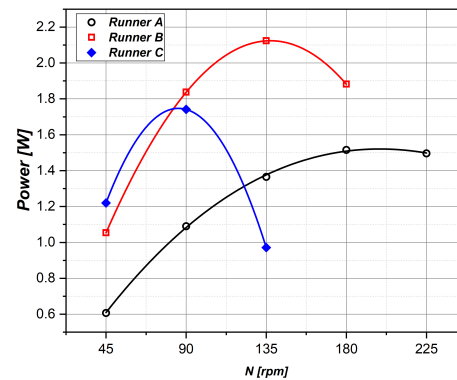
4.1   The effect of Runner diameter to Basin diameter Ratio

This section presents the result of CFD analysis performed for simulation based on the variation of runner outer diameter. The size of runner blades are defined by runner outer diameter as discussed in Section 2.2. This presents the results of CFD analysis for three runner sizes namely: Runner A, Runner B and Runner C. The outer diameter of Runner A blades is 90 mm or 10 mm larger than the diameter of discharge hole means the size of Runner A blades are located in the discharge region, the outer diameter of Runner B blades is 135 mm or 55 mm larger than the orifice diameter means the size of Runner B blades are located in the near–field region and the outer diameter of Runner C blades is 180 mm or 100 mm larger that the orifice diameter means the size of Runner C blades are extended into the far–field region. The variation of runner outer diameter can be expressed by the ratio of runner diameter to basin diameter (R). The ratio of runner diameter to basin diameter for Runner A, Runner B and Runner C are $R = 0.18$, $R = 0.27$ and $R = 0.36$ respectively. The simulations are performed for each runner at each input runner rotational speed varying from 45 rpm until the rotational speed where the power output and runner efficiency reaches maximum and tends to decrease.
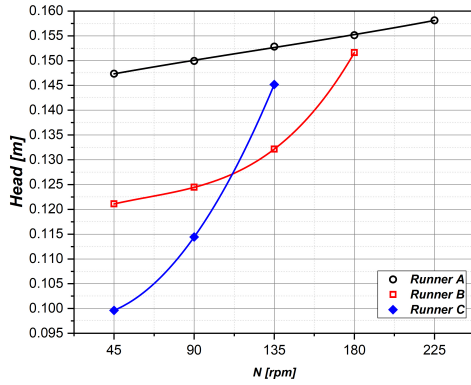
Figure 13 presents the performance comparison for all runners. The higher torque is produced by Runner C with steep decreasing rate as in Fig. 13a. The maximum power output on data fit curves is 1.52 W at 189.9 rpm for Runner A, 2.12 W at 137.4 rpm for Runner B and 1.75 W at 85.6 rpm for Runner C. It shows that Runner B has more power output than Runner A and Runner C.
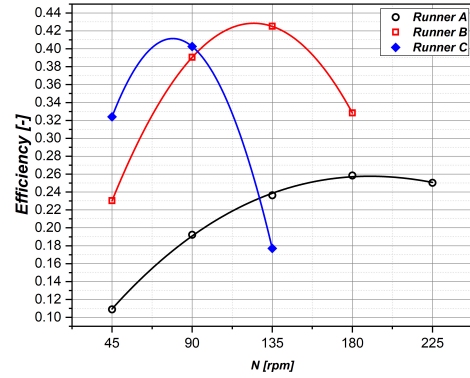

(a) Torque

(b) Power output

19

(c) *Effective head*

(d) *Runner efficiency*

Figure 13: *Runner performance comparison for variable runner diameter to basin diameter ratio (R):*
R = 0.18 for Runner A, R = 0.27 for Runner B and R = 0.36 for Runner C

Figure 13c shows that the height of water in basin is high for Runner A as compared with Runner B and Runner C. The efficiency curves are also illustrated in Fig. 13d. The maximum efficiency achieved for Runner A, Runner B and Runner C were 25.8%, 42.9% and 41.2% respectively. This study found that Runner B has higher performance than Runner A and Runner C. For detail explanation Runner A has higher rotational speed due to the strength of vortex was higher in the vicinity of air core but produces less torque. Runner C has less rotational speed and high torque due to larger blade sizes. However, Runner B produces more power and efficiency as compared to Runner C due to the nature of vortex tangential velocity field decrease with increasing radius. In addition this work identified extending the size of runner blades to the far–field region resulting in reduction of power output.

Figure 14 presents the flow field visualization for tangential velocity and water free–surface for each runner at their rotational speed where the power output and the runner efficiency took the maximum values. Figures 14a to 14c shows that the water free–surface entrained through the discharge hole which indicates the presence of air–core (air entrainment) for aeration. Moreover, the height of vortex decreases with an increase in blade size and this finding is similar to Power et al. (2016).
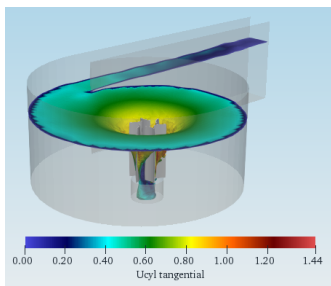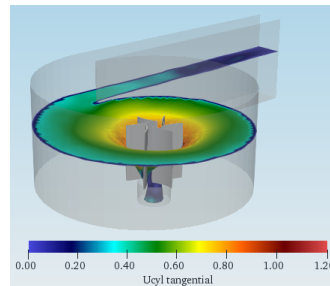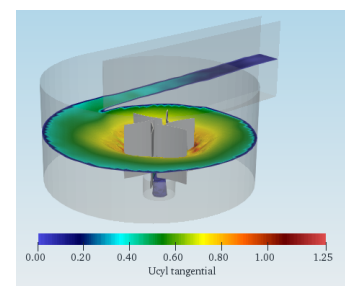

(a) *Runner A at N = 180 rpm*

(b) *Runner B at N = 135 rpm*

(c) *Runner C at N = 90 rpm*

Figure 14: *Water free–surface with tangential velocity contour*

20

5 Conclusions

In the present study, a detailed CFD analysis was performed on the runner optimization to explore the characteristic of runner–vortex interaction and the effect of the ratio of runner diameter to basin diameter on the power output and efficiency. As a result, increasing the size of runner blades from the vicinity of orifice to the near–field region increases the power output and efficiency of the runner. However, extending the size of runner blades to the far–field region resulted reduction in performance of the runner. The maximum power output and efficiency was obtained by Runner B with the runner diameter in the near–field region. A comprehensive experimental study is suggested to validate the outcomes of the current study which will be helpful to design and establish performance analysis for the Gravitational Water Vortex Power Plant for a given flow and head of particular hydropower site. Moreover, it can also be used as pointer for the future generations of Gravitational Water Vortex Turbine technology.

Acknowledgment

Nomenclature

List of abbreviations

CAD	Computer Aided Design
CC	Curvature Correction
CFD	Computational Fluid Dynamics
CFL	Courant Friedrich Levy
FVM	Finite Volume Method
GWVPP	Gravitational Water Vortex Power Plant
GWVT	Gravitational Water Vortex Turbine
IEA	International Energy Agency
MMPH	Mini, Micro, and Pico Hydropower
MRF	Multiple Reference Frame
OpenFOAM	Open Field Operation and Manipulation
RANS	Reynolds Averaged Navier-Stokes
RSM	Reynolds Stress Model
SM	Sliding Mesh
SST	Shear Stress Transport
VOF	Volume of Fluid

Greek letters

α	volume fraction	$[-]$
δ	The clearance between basin base and runner base	$[mm]$
η_t	Turbine efficiency	
κ	Free–surface curvature	
μ	Dynamic viscosity	$[m^2.s^{-2}]$
μ_t	Turbulent viscosity	$[m^2.s^{-2}]$
μ_{eff}	Effective viscosity	$[m^2.s^{-1}]$
∇	Gradient operator	
$\nabla.$	Divergence operator	
ν	Kinematic viscosity	$[m^2.s^{-1}]$
ω	Specific dissipation rate	$[s^{-1}]$
ρ	Fluid density	$[kg.m^{-3}]$
σ	Surface tension	$[kg.s^2]$
ε	Eddy viscosity	$[m^2.s^{-3}]$
k	Turbulent kinetic energy	$[m^2.s^{-2}]$

List of symbols

$\bar{p}$	Time–averaged pressure	$[kg.m.s^{-2}]$
$\bar{\mathbf{u}}_\mathbf{r}$	Artificial compression velocity	$[m.s^{-1}]$
$\mathbf{g}$	Acceleration due to gravity	$[m.s^{-2}]$
$\mathbf{h}$	The position vector	$[m]$
$\mathbf{n}$	Normal vector	

21

$\bar{\mathbf{u}}$	Time–averaged velocity	$[m.s^{-1}]$	p	Pressure	$[kg.m.s^{-2}]$
$\mathbf{u}$	Velocity	$[m.s^{-1}]$	p'	Fluctuating pressure	$[kg.m.s^{-2}]$
$\mathbf{u'}$	Fluctuating velocity	$[m.s^{-1}]$	P_{in}	The hydraulic power input	$[kg.m^2.s^{-3}]$
ω	The runner angular velocity	$[s^{-1}]$	P_{out}	The mechanical power output	$[kg.m^2.s^{-3}]$
θ_c	The blade deflection angle	$[deg]$	Q	Volumetric flow rate	$[m^3.s^{-1}]$
B_h	The runner blade height	$[m]$	R	Runner diameter to Basin diameter ration	$[-]$
b_i	Channel width	$[m]$	r	Radial position from the orifice center	$[m]$
B_t	The runner blade thickness	$[m]$	r_c	The blade radius of curvature	$[m]$
Co	Courant number		$r_i = D_i/2$	The runner inner radius	$[m]$
D	Basin diameter	$[m]$	$r_o = D_o/2$	The runner outer radius	$[m]$
d	Orifice diameter	$[m]$	r_{in}	Radial distance from orifice center to inlet channel mid	$[m]$
D_i	Runner inner diameter	$[m]$			
D_o	Runner outer diameter	$[m]$	T	Torque	$[Nm]$
h	Channel depth	$[m]$	t	time	$[s]$
H_g	Gross Head	$[m]$	Z	Number of Blades	$[-]$
$H_n\ (H)$	Effective or Net Head	$[m]$	**Subscripts**		
H_t	Turbine work head	$[m]$	g	Gas	
L_B	Channel length	$[m]$	in	inlet	
L_o	Orifice length	$[m]$	l	Liquid	
N	Rotational speed	$[rpm]$	out	Outlet	

References

Bajracharya, T. and Chaulagai, R. (2012). Developing innovative low head water turbine for free–flowing streams suitable for micro hydropower in flat (terai) regions in nepal.

Bajracharya, T. R., Shakya, S. R., Timilsina, A. B., Dhakal, J., Neupane, S., Gautam, A., and Sapkota, A. (2020). Effects of Geometrical Parameters in Gravitational Water Vortex Turbines with Conical Basin. *Journal of Renewable Energy*, page 16, DOI: 10.1155/2020/5373784.

Chattha, J. A., Cheema, T. A., and Khan, N. H. (2017). Numerical investigation of basin geometries for vortex generation in a gravitational water vortex power plant. In *8th International Renewable Energy Congress, (IREC 2017)*. DOI: 10.1109/IREC.2017.7926028.

Christopher, J. G. (2018). OpenFOAM User Guide, version 6.

Dhakal, R., Bajracharya, T., Shakya, S., Kumal, B., Williamson, S. J., Guatam, S., Ghale, D., and Khanal, K. (2017). Computational and experimental investigation of Runner for Gravitational Water Vortex Power Plant. In *6th International Conference on Renewable Energy Research and Applications*, volume 5, pages 365–373.

Dhakal, S., Nakarmi, S., Pun, P., Thapa, A. B., and Bajracharya, T. R. (2013). Development and Testing of Runner and Conical Basin for Gravitational Water Vortex Power Plant. *Journal of the Institute of Engineering*, 10(1):140–148, DOI: 10.3126/jie.v10i1.10895.

Dhakal, S., Timilsina, A. B., Dhakal, R., Fuyal, D., Bajracharya, T. R., Pandit, H. P., Amatya, N., and Nakarmi, A. M. (2015). Comparison of cylindrical and conical basins with optimum position of runner: Gravitational water vortex power plant. *Renewable and Sustainable Energy Reviews*, 48:662–669, DOI: 10.1016/j.rser.2015.04.030.

Drioli, C. (1947). Su un particolare tipo di imbocco per pozzi di scarico (scaricatore idraulico a vortice). *L'Energia Elettrica*, 24(10):447–452.

Ferziger, J. H. and Peric, M. (2002). *Computational Methods for Fluid Dynamics*. Springer, 3rd edition.

Foundation, O. (2020). OpenFOAM C++ Documentation. http://openfoam.org/docs/cpp/. [Accessed: 01 Mar 2020].

Freitas, C. J. (2002). The issue of numerical uncertainty. *Applied Mathematical Modelling*, 26(2):237–248.

Gullberg, P. and Sengupta, R. (2011). Axial fan performance predictions in CFD, comparison of MRF and sliding mesh with experiments. In *Proceedings of the SAE 2011 World Congress and Exhibition*.

Hirt, C. W. and Nichols, B. D. (1981). Volume of Fluid (VOF) Method for the Dynamics of Free Boundaries. *Journal of Computational Physics*, 39(1):201–225.

Hoes, O. A., Meijer, L. J., Van Der Ent, R. J., and Van De Giesen, N. C. (2017). Systematic high-resolution assessment of global hydropower potential. *PLoS ONE*, 12(2):1–10, DOI: 10.1371/journal.pone.0171844.

IEA (2018). Global Energy & CO2 Status Report: The latest trends in energy and emissions in 2018. Technical report.

Kayastha, M., Raut, P., Kumar, N., Sandesh, S., Ghising, T., and Dhakal, R. (2019). CFD evaluation of performance of Gravitational Water Vortex Turbine at different runner positions. In *Kantipur Engineering College (KEC) Conference*, pages 17–25.

Khan, N. H. (2016). Blade Optimization of Gravitational Water Vortex Turbine. Msc. thesis, Ghulam Ishaq Khan Institute of Engineering Sciences and Technology.

Kueh, T. C., Beh, S. L., Rilling, D., and Ooi, Y. (2017). Experimental study to the influences of rotational speed and blade shape on water vortex turbine performance. In *Journal of Physics: Conference Series*, volume 755. DOI: 10.1088/1742-6596/755/1/011001.

Marian, G.-M., Sajin, U., Florescu, I., Nedelcu, D.-I., and Ostahie (2012). The Concept and Theoretical Study of Micro Hydropower Plant With Gravitational Vortex and Turbine Turbine With Rapidity Steps. *Buletinul AGIR*, 3(3):219–226.

Menter, F., Kuntz, M., and Langtry, R. (2003). Ten years of industrial experience with the SST turbulence model. *Turbulence, Heat and Mass Transfer*, 4:625–632.

Mühle, F., Rapp, C., and Mayer, O. (2013). Experimentelle untersuchungen an einem wasserwirbel-kraftwerk. *WASSERWIRTSCHAFT*, 103:41–46, DOI: 10.1365/s35147-013-0649-y.

Müller, S., Cleynen, O., Hoerner, S., Lichtenberg, N., and Thévenin, D. (2018). Numerical analysis of the compromise between power output and fish-friendliness in a vortex power plant. *Journal of Ecohydraulics*, 3(2):86–98, DOI: 10.1080/24705357.2018.1521709.

Mulligan, S. and Casserly, J. (2010). The hydraulic design and optimisation of a free water vortex for the purpose of power extraction.

Mulligan, S., Casserly, J., and Sherlock, R. (2012). Numerical and experimental modeling of the water surface in a vortex hydroelectric plant in the absence of a turbine impeller. In *Proceedings of the 23rd conference of hydraulics and hydraulic engineering*, Brescia, Italy.

Mulligan, S., Casserly, J., and Sherlock, R. (2016). Experimental and Numerical Modelling of Free-Surface Turbulent Flows in Full Air-Core Water Vortices. *Advances in Hydroinformatics*, 9:549–569, DOI: 10.1007/978-981-287-615-7.

Mulligan, S., Creedon, L., Casserly, J., and Sherlock, R. (2018). An improved model for the tangential velocity distribution in strong free-surface vortices: an experimental and theoretical study. *Journal of Hydraulic Research*, 57(4):547–560, DOI: 10.1080/00221686.2018.1499050.

Mulligan, S. and Hull, P. (2011). Design and Optimisation of a Water Vortex Hydropower Plant.

Nishi, Y. and Inagaki, T. (2017). Performance and Flow Field of a Gravitation Vortex Type Water Turbine. *International Journal of Rotating Machinery*, DOI: 10.1155/2017/2610508.

Nishi, Y., Suzuo, R., Sukemori, D., and Inagaki, T. (2020). Loss analysis of gravitation vortex type water turbine and influence of flow rate on the turbine's performance. *Renewable Energy*, 155:1103–1117, DOI: 10.1016/j.renene.2020.03.186.

Power, C., McNabola, A., and Coughlan, P. (2016). A Parametric Experimental Investigation of the Operating Conditions of Gravitational Vortex Hydropower (GVHP). *Journal of Clean Energy Technologies*, 4(2):112–119, DOI: 10.7763/jocet.2016.v4.263.

Rahman, M., Hong, T. J., Tang, R., and Sung, L. L. (2016). Experimental Study the Effects of Water Pressure and Turbine Blade Lengths & Numbers on the Model Free Vortex Power Generation System. *International Journal of Current Trends in Engineering & Research*, 2(9):13–17.

Rahman, M. M., Hong, T. J., and Tamiri, F. M. (2018). Effects of inlet flow rate and penstock's geometry on the performance of Gravitational Water Vortex Power Plant. In *Proceedings of the International Conference on Industrial Engineering and Operations Management*, pages 2968–2976.

Rahman, M. M., Tan, J. H., Fadzlita, M. T., and Wan Khairul Muzammil, A. R. (2017). A Review on the Development of Gravitational Water Vortex Power Plant as Alternative Renewable Energy Resources. In *IOP Conference Series: Materials Science and Engineering*, volume 217. DOI: 10.1088/1757-899X/217/1/012007.

Ramos, H. M., Simão, M., and Kenov, K. N. (2012). Low-Head Energy Conversion: A Conceptual Design and Laboratory Investigation of a Microtubular Hydro Propeller. *ISRN Mechanical Engineering*, pages 1–10, DOI: 10.5402/2012/846206.

Regmi, N., Dura, H., and Shakya, S. R. (2019). Design and Analysis of Gravitational Water Vortex Basin and Runner. volume 7, pages 157–164.

REN21 (2018). Renewables 2018 global status report. Technical report, http://www.ren21.net/status-of-renewables/global-status-report/.

Sánchez, A. R., Rio, J. A. S. D., Muñoz, A. J. G., and Montoya, J. A. P. (2019). Numerical and Experimental Evaluation of Concave and Convex Designs for Gravitational Water Vortex Turbine. *Journal of Advanced Research in Fluid Mechanics and Thermal Sciences*, 64(1):160–172.

Santiago, M. D. (2004). Description and utilization of interFoam multiphase solver.

Smirnov, P. and Menter, F. (2009). Sensitization of the SST turbulence model to rotation and curvature by applying the Spalart-Shur correction term. *J. Turbomach.*, 131(4).

Timilsina, A. B., Mulligan, S., and Bajracharya, T. R. (2018). Water vortex hydropower technology: a state-of-the-art review of developmental trends. *Clean Technologies and Environmental Policy*, 20(8):1737–1760, DOI: 10.1007/s10098-018-1589-0.

Tonello, N., Eude, Y., de Laage de Meux, B., and Ferrand, M. (2017). Frozen rotor and sliding mesh models applied to the 3D simulation of the Francis-99 Tokke turbine with Code Saturne. *Journal of Physics: Conference Series*, 782.

Turbulent (2020). Technology–Turbulent Website. https://www.turbulent.be/technology/. [Accessed: 01 Mar 2020].

Ullah, R., Cheema, T. A., Saleem, A. S., Ahmad, S. M., Chattha, J. A., and Park, C. W. (2019). Performance analysis of multi-stage gravitational water vortex turbine. *Energy Conversion and Management*, 198, DOI: 10.1016/j.enconman.2019.111788.

Versteeg, H. K. and Malalasekera, W. (2007). *An introduction to Computational Fluid Dynamics*. Pearson/Prentice Hall, 2nd edition.

Wilhelm, D. (2015). Rotating Flow Simulations with OpenFOAM. *International Journal of Aeronautical Science & Aerospace Research (IJASAR)*, pages 1–7.

Williamson, S. J., Stark, B. H., and Booker, J. D. (2014). Low head pico hydro turbine selection using a multi-criteria analysis. *Renewable Energy*, 61:43–50, DOI: 10.1016/j.renene.2012.06.020.

World Bank (2006). Technical and economic assessment of off-grid, Mini-grid and grid electrification technologies. Technical report.

Zotlöterer, F. (2004). Hydroelectric Power Plant. WO2004061295A2.

Zotlöterer, F. (2008). Water Vortex Power Plant. WO2008141349A2.

Zotlöterer, F. (2020). Gravitation water vortex power plants. http://www.zotloeterer.com/welcome/gravitation-water-vortex-power-plants/. [Accessed: 29 Feb 2020].